The Astrophysical Journal, 592:597–606, 2003 July 20

CORONAL STRUCTURE OF A FLARING REGION AND ASSOCIATED CORONAL MASS EJECTION

P. K. Manoharan[1,2] and M. R. Kundu
Department of Astronomy, University of Maryland, College Park, MD 20742
Received 2002 August 30; accepted 2003 April 2

ABSTRACT

We report the multiwavelength investigations of an eruptive flare event that occurred on 2001 April 2 at about 11 UT. The manifestations associated with this flare event have been studied from the near-Sun region to about 0.5 AU. The Hα images from the Meudon Spectroheliograph reveal a fast spectacular eruption of plasmoids from the flare site to the west and a Moreton wave disturbance propagating toward the south. A bright, fast, wide coronal mass ejection (CME) associated with this eruptive event was imaged by *SOHO*/LASCO and the remote-sensing interplanetary scintillation technique. The radio measurements from the Nançay Radioheliograph and Tremsdorf Radio Telescope have been useful in identifying the radio signatures of the CME's initiation. The metric type II radio bursts produced at the time of CME onset also propagate toward the west, and their positions coincide with the magnetic null point, which was located at the southwest part of NOAA active region 9393. The timings and positions of the radio bursts, the Hα eruption, and the CME onset as well as the magnetic field configuration suggest a release of energy at the null point, and as indicated by the Moreton wave, the eruption starts close to the chromospheric or low coronal level. The results support the "breakout" scenario proposed by S. Antiochos and coworkers, and they are also suggestive that the energy release is followed by magnetic reconnection between the low-lying loops near the separatrix and the loop system above them.

Subject headings: Sun: coronal mass ejections (CMEs) — Sun: flares — Sun: magnetic fields — Sun: radio radiation

On-line material: color figures

1. INTRODUCTION

Coronal mass ejections (CMEs) are large expulsions of mass and magnetic field from the Sun into the heliosphere. They are responsible for nonrecurrent disturbances in the interplanetary medium, and their interactions with Earth's magnetosphere cause severe geoeffective storms. These mass ejections carry a bulk of solar material in the range 10^{11}–10^{14} kg at speeds of 10–2000 km s^{-1}. The huge amount of energy involved in such ejection processes is believed to be stored in the magnetic fields surrounding the mass ejection site. An understanding of the coronal magnetic field configuration and its spatial and temporal evolution is therefore essential in diagnosing the energy release mechanism (or process). However, since it is difficult to measure the coronal fields directly from observations, the photospheric measurements of the field pattern and the detection and analysis of other manifestations produced during the process of energy release (such as Hα eruption, radio, microwave, extreme-ultraviolet, X-rays, shock propagation, and particle events) can provide diagnostics on various stages of the eruption of a CME. For example, the analysis using high-resolution images of the Sun observed over a wide range of wavelengths contributed to enhance our understanding of the solar atmosphere during a flare process (e.g., Kundu et al. 2001).

On the theoretical aspect of energy release/mass ejection, a wide variety of magnetic models have been proposed to explain and interpret the CME observations in the near-Sun region as well as in the interplanetary space (e.g., see review by Hudson 1999). But most of the models tend to imitate closely and explain the white-light measurements of CMEs, and there is an exceedingly large gap between the available models and observable quantities of a CME at the near Sun (e.g., "sheared-core" models; Moore et al. 2001). In a recent model proposed by S. Antiochos and coworkers (Antiochos, DeVore, & Klimchuk 1999), it is argued that in a complex magnetic configuration, the accumulation of energy continues at the lower atmosphere of the Sun until a "breakout" or reconnection occurs above the energy storage point.

In this paper, we report a multiwavelength study of an X1.1 flare event that occurred on 2001 April 2. This flare took place at the southwest part of NOAA active region 9393, which unleashed several intense flares during 2001 March–April and was the largest sunspot group of the current solar cycle. Associated with this flare event, a bright, fast, wide CME was observed. Since the flare occurred when the active region was close to the west limb of the Sun (i.e., $\sim$N10°, W65°), it provided an opportunity to study the characteristics of the CME in detail. The information about the near solar surface manifestations of the eruption was obtained from Hα spectroheliograms. The on-disk signatures of the initial phase of the CME onset and its near-Sun characteristics are from radio observations over the frequency range of 1–800 MHz. We compare our observational results of the CME onset with the three-dimensional magnetic field configuration obtained from the force-free extrapolation method. The paper is organized as follows. In § 2 we describe the X-ray, Hα, and radio observations in the initial phase of the eruption. Section 3 discusses the interplanetary propagation effects of the CME. In § 4, we present the results of magnetic field extrapolation obtained from the

[1] Center for Solar Physics and Space Weather, Catholic University of America, Washington, DC 20064.

[2] On sabbatical leave from Tata Institute of Fundamental Research, Radio Astronomy Centre, Ooty (Udhagamandalam), India.

magnetogram and extreme-ultraviolet images of the Sun, and the results are compared and discussed in the context of observational findings.

2. OBSERVATIONS

The soft X-ray measurements by *GOES* satellite reveal this flare to be a typical long-duration event lasting from 10:50 to 12:00 UT, with a maximum around 11:30 UT. Figure 1 shows the X-ray emission as recorded by *GOES 8* in the 1–8 Å and 0.5–4 Å channels. In these profiles of X-ray intensity, one may notice the superposition of two peaks near the maximum of the curve. The first peak and a sudden increase in intensity occur, respectively, at ~11:23 and 11:27 UT. The change in intensity levels of these peaks may be seen in the harder X-ray emission channel of *GOES*.

2.1. Hα *Images: Plasmoid Eruption*

We first attempt to identify the features related to the start of the CME in the Hα data. The Hα measurements reported in this paper are from the Meudon Spectroheliograph, which routinely makes full-disk images of the Sun at the Hα line center and at 0.5 Å shift in wavelength on either side of the center. The Hα images used in this study have a spatial resolution of $\sim 2''$ pixel^{-1} and temporal cadence of ~1 minute (J.-M. Malherbe 2002, private communication).

The Hα light curve inferred from the CCD count rate showed a gradual rise and fall between 11:00 and 11:50 UT, with a distinct peak at 11:27 UT. Although the overall intensity of this event in Hα was not significantly bright, a careful examination and analysis of the high-cadence Meudon images using the running subtraction method revealed a fast spectacular eruption of blobs of material from the active region site. Most of the eruption in Hα was observed during the rising phase of its intensity between 11:00 and 11:27 UT. During this time period, a cusplike rising loop structure was observed at the flaring region and a Moreton wave propagated from the flare site to the south along the surface of the Sun. In front of the cusp, material in the form of blobs flowed westward. We could follow the tracks of three blobs at the position angle P.A. $\approx 290°$, starting from a height of 0.9 to 1.1 $R_\odot$ in the sky plane (solar radius $R_\odot = 6.96 \times 10^5$ km). Figure 2 shows some representative images of the eruption and propagation of the Moreton wave as seen in Hα. These are the running difference images, and the wave and material in the form of blobs moving radially outward can be seen in the figure. Note that these blobs were not formed at the same time or at the same height. But they were formed one after another at increasing heights. Figure 3 shows the tracks of these blobs on the height-time plot. It is evident from their tracks that all three blobs showed considerable acceleration while ascending, and their average speeds were 90, 165, and 190 km s^{-1}. The successive blobs thus showed an increase in their average speed and acceleration with height (or time). Since the height-time plot is likely to represent the projected distance, the quantities (i.e., speed and acceleration) derived from it correspond to lower limits of these quantities.

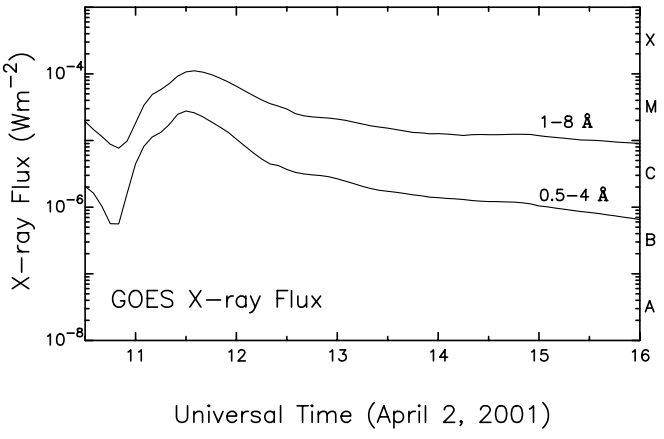

FIG. 1.—Soft X-ray light curves from *GOES 8* spacecraft for the period 10:30–16:00 UT. The upper curve is from the 1–8 Å channel of *GOES* and the lower curve is from the 0.5–4 Å channel. The soft X-ray flare levels are indicated on the right-hand side of the plot.

2.2. *Radio Images and Spectra:* 1–800 MHz *Data*

To study various stages of this eruptive event in the low as well high corona, we use both radio spectral data and two-dimensional radio images of the Sun. The high time resolution images of the Sun are routinely made at the Nançay Radioheliograph (NRH), which operates in the frequency range of 160–435 MHz and probes the coronal plasma at heights $\leq 1.5\ R_\odot$. A full description of the NRH is given by Kerdraon & Delouis (1997). In the above frequency range, before the Hα eruption, two dominant radio sources were observed close to the west limb. The first source was located near the equatorial region (source A), and the other occupied the position around the mid–northern latitude of the solar west limb (source B), and these radio sources showed systematic height variation with observing frequencies as shown in Figure 4. Images displayed in Figure 4 show the preeruption conditions recorded by the NRH systems at 164–410 MHz, the *SOHO* Extreme Ultraviolet Imaging Telescope (EIT) instrument at 195 Å, and the *SOHO* Michelson Doppler Imager (MDI) magnetometer. The EIT and MDI images have been observed at ~09:36 UT and the radio images in the time interval of 10:45–10:55 UT on 2001 April 2. For one-to-one comparison, these images have been scaled and plotted on the same photospheric-disk radius, and each of them covers in the east-west direction from the central meridian to the west limb and farther west and in the north-south direction from 0.3 $R_\odot$ south of the disk center to the north pole and above. The west limb is marked on radio images by a continuous line, and the vertical dotted lines plotted on them show the boundaries of the size of the plotted radio image at a given observing frequency.

Bright and faint loop systems evidently seen in the EIT data and their corresponding magnetic structures are given by the MDI magnetogram. A system of faint loops at the north side of the active region seen in the EIT image has also been revealed by the magnetic field extrapolation discussed in § 4 (Figs. 11 and 12*a*). When we examined the location of the strong emitting region during the time of eruption between 11:00 and 11:20 UT, it was inferred from the EIT data that most of the activity occurred close to the southwest end of the active region, where a bright-loop leg was anchored. It is also consistent with the brightness and position of the radio-emitting region. A majority of the transient radio activities occurred close to or in the vicinity of source A, which was located radially above the southwest of the active region. On account of the projection effect, the

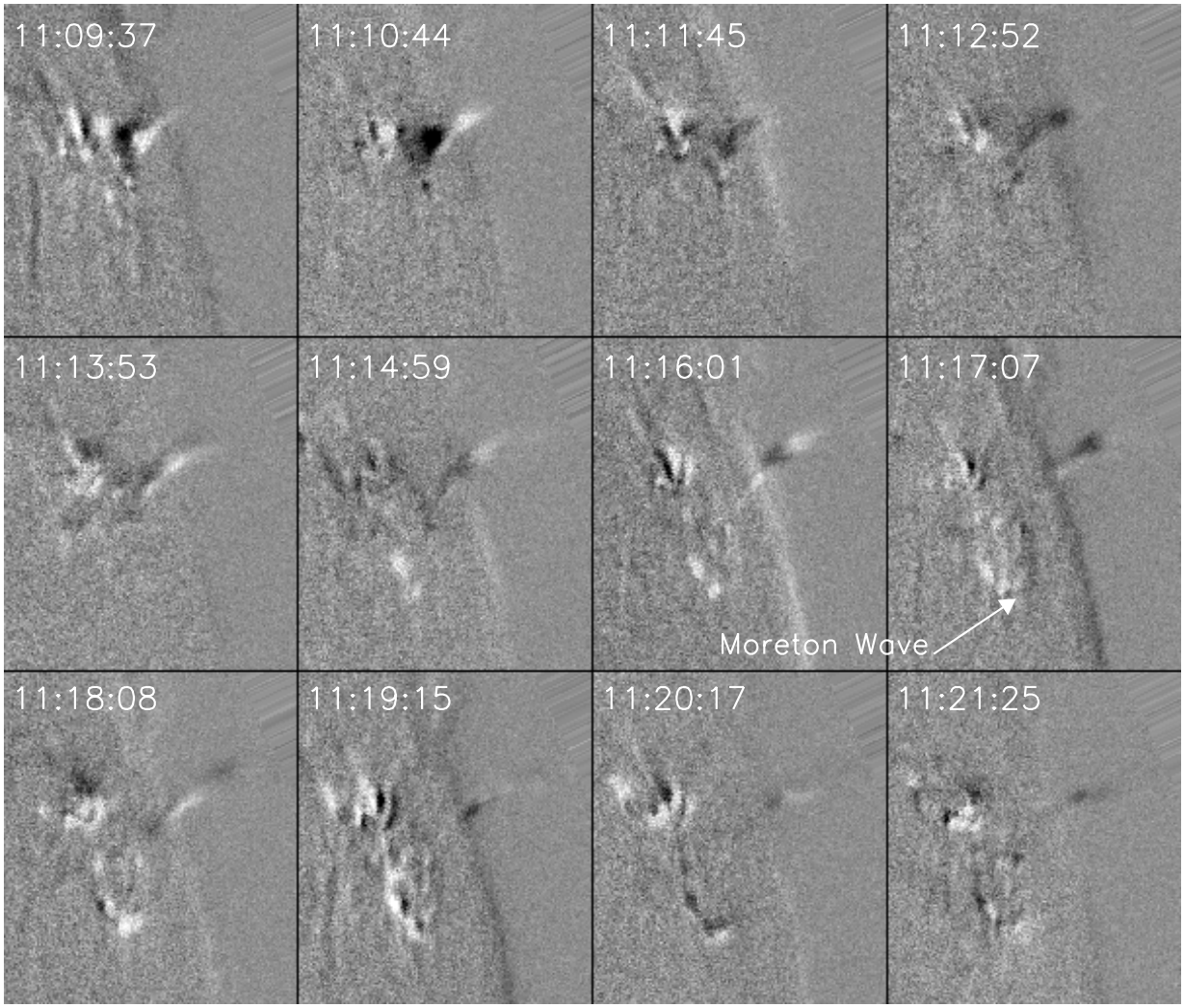

FIG. 2.—Northwest portion of the full-disk images of the Sun observed in Hα showing the eruption. The westward-moving bloblike structure and southward-propagating Moreton wave are indicated. The size of the image is 150 × 170 pixels, where each pixel is about 2″. The west limb of the Sun can also be seen in these images.

low-frequency emission height of this source appears off the west limb of the photosphere. The radio images shown in Figure 4 explain the height evolution of radio sources A and B with decreasing frequency (i.e., with increasing height of plasma emission above the photosphere). A plot included at the lower right end of Figure 4 shows the offset of sources A and B from the disk center as a function of observing frequency; for comparison, as seen in the EIT image, the positions of southwest end and north edge of the active region with respect to the disk center are also plotted at 500 MHz. The systematic increase in separation between radio sources A and B as well as the height of source A indicate that these two sources likely belong to the same system of loops running across the active region. In the onset phase of the CME, around 11:02 UT, type III radio bursts were observed, and they were also located close to the eastern edge of source A, implying the existence of open field lines in this location.

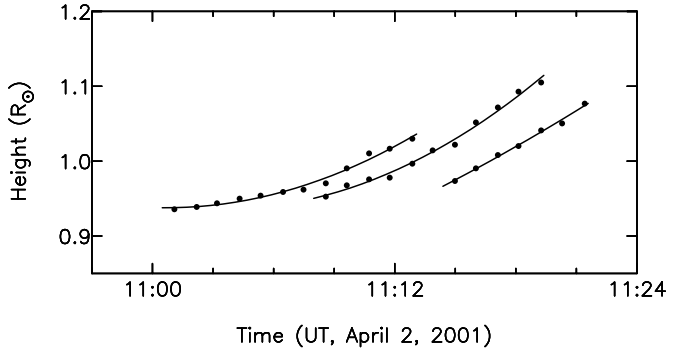

FIG. 3.—Height-time plot of Hα blobs observed during 11:00–11:24 UT. The continuous line is the best fit to the each blob's data points. It is evident that all three blobs show acceleration. Average speeds of these tracks from left to right are 90, 165, and 190 km s^{-1}.

Figure 5 shows the radio flux density profiles observed over the northwest quarter of the NRH image (e.g., the portion of the NRH image shown in Fig. 4) at five discrete frequencies, 164, 236, 327, 410, and 432 MHz, between 10:40 and 12:20 UT on 2001 April 2. These profiles have been arranged for convenience along the flux-density axis and plotted on a single graph to show the relative variations in the measured radio emission. The radio flux density is given

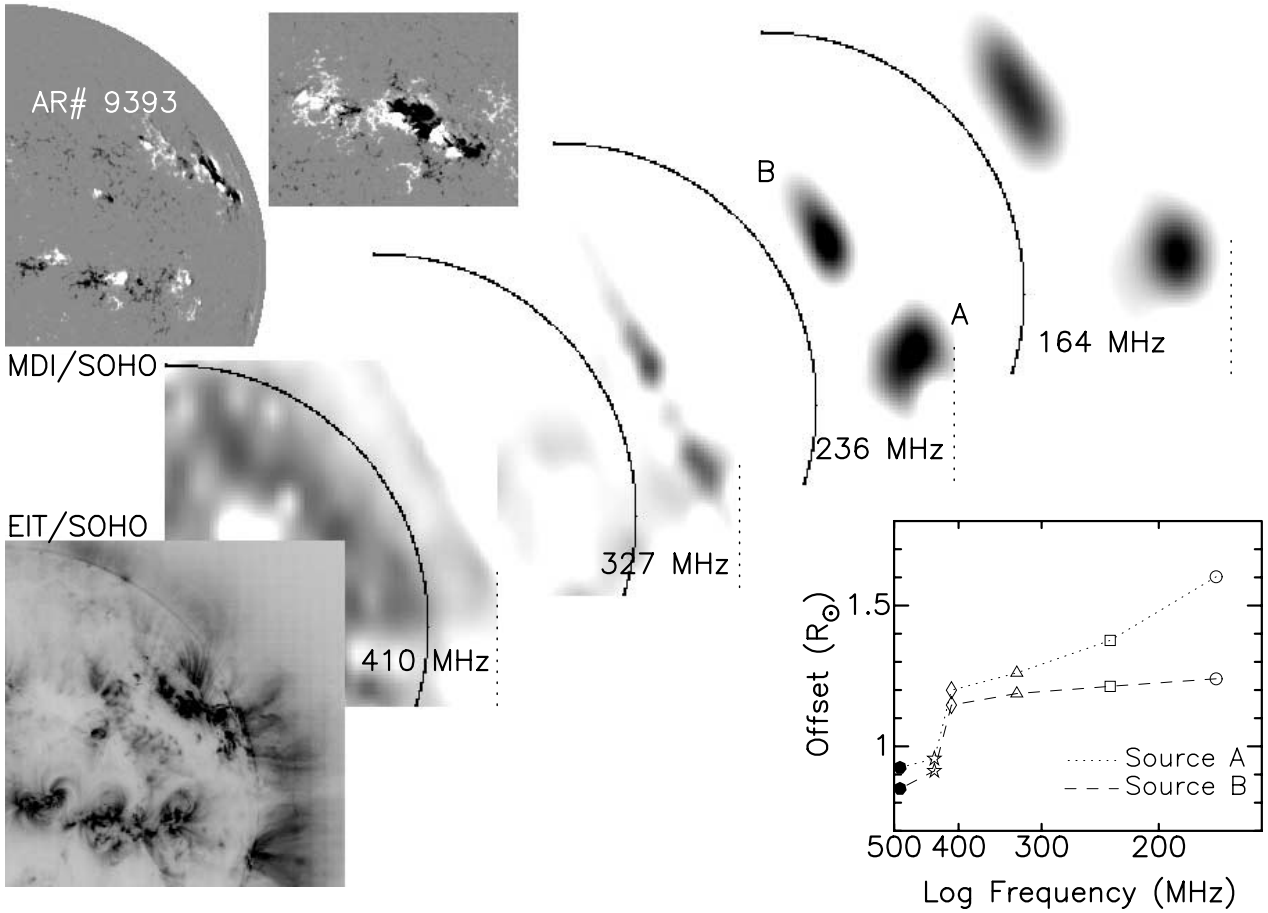

FIG. 4.—Northwest quarter of MDI, EIT, and radio images of the Sun during preeruption. The EIT image (at 09:36 UT) and MDI image at the left (at 09:36 UT) and the radio images (in the time interval 10:45–10:55 UT) have been observed on 2001 April 2. The MDI image on the right shows the view of the magnetic configuration of the active region when it was close to the central meridian on 2001 March 29, at 11:12 UT. On radio images, the west limb is marked by a continuous line, and the vertical dotted lines plotted on them show the boundaries of the size of the radio image at a given observing frequency. The plot at the lower right corner shows the offsets of sources A and B from the disk center as the function of observing frequency. During the eruption, the radiation at the metric wavelengths was dominated by the emission from the radio source A, which was located radially above the magnetic null point (see § 4). The EIT positions of southwest end and north edge of the active region with respect to the disk center are plotted at 500 MHz. [*See the electronic edition of the Journal for a color version of this figure.*]

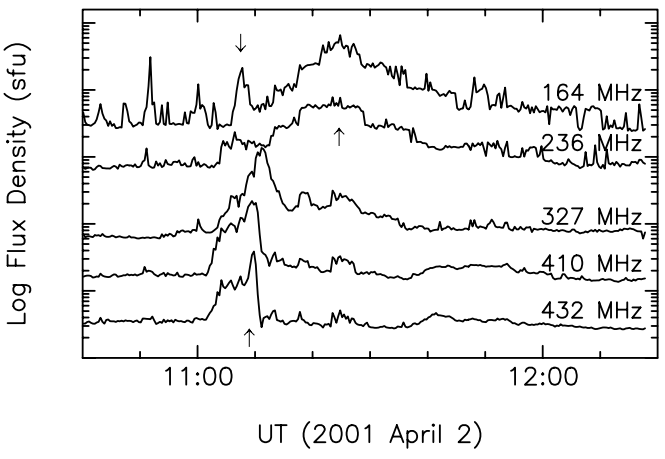

FIG. 5.—Time profiles of radio flux density observed at all five frequency bands of the NRH. Each profile represents radio flux density integrated over the northwest quarter of the NRH image as shown in Fig. 4. The up and down arrows plotted between 11:00 and 11:10 UT indicate, respectively, fast- and slow-drifting type II bursts. The approximate midpoint of the moving type IV burst at 164 MHz is shown by an arrow symbol at ~11:25 UT.

in solar flux units (1 sfu = 10^4 Jy). Figure 5 illustrates the time sequence of various radio bursts associated with the flare, and a comparison of these flux density profiles with the radio spectrogram provides a detailed understanding of the eruption and the CME onset.

Figure 6 shows the combined dynamic radio spectrum obtained from the ground-based Tremsdorf Radio Telescope[3] and space mission *Wind*/WAVES,[4] respectively, in the frequency range of 40–800 MHz and 1–13.8 MHz. This is a gray-scale plot of observed radio intensity plotted as function of frequency and time (in the electronic version of the figure, red color indicates the intense emission). The Tremsdorf spectrum (40–800 MHz) reveals the conditions of the coronal plasma at heights less than ~2 $R_\odot$, whereas the WAVES instrument probes plasma at heights larger than the above and up to about 10 $R_\odot$. The following components are evident from the radio spectrum: (1) type III

[3] For more information on the Tremsdorf Radio Telescope, see http://www.aip.de/groups/osra/.

[4] For more information on the space mission *Wind*/WAVES, see http://lep694.gsfc.nasa.gov/waves/waves.html.

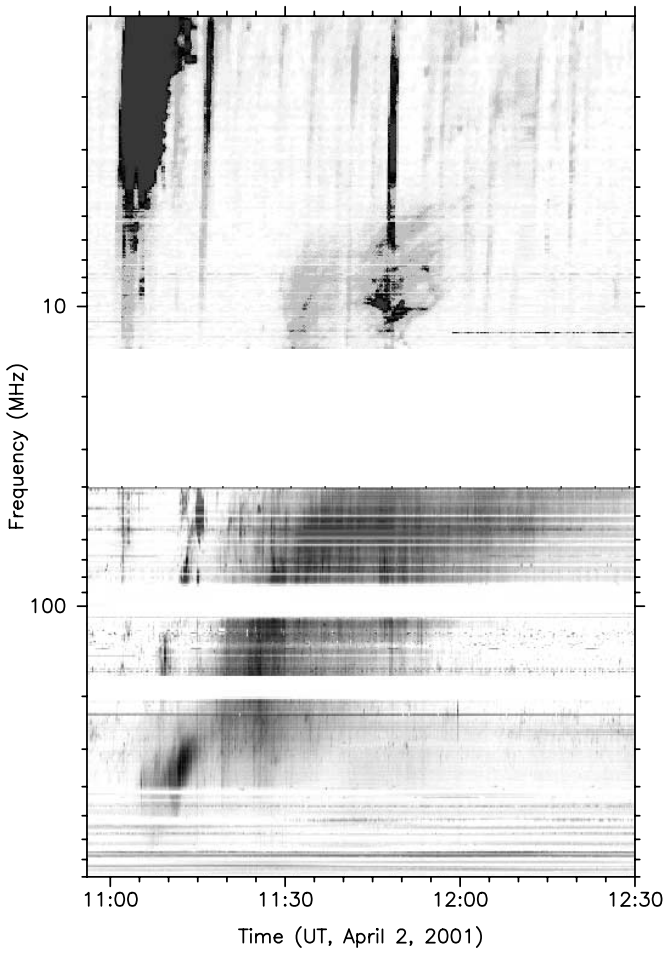

FIG. 6.—Composite radio dynamic spectrum in the frequency range of 1–800 MHz, constructed from the spectra obtained from *Wind*/WAVES and from the spectrometer at Potsdam, Tremsdorf. The frequency of ~1 MHz at the top of the spectrum increases in the downward direction to ~800 MHz. [*See the electronic edition of the Journal for a color version of this figure.*]

bursts observed around 11:02 UT starting at a frequency of ~160 MHz, continuing in the rest of the low-frequency band of the Tremsdorf spectrum and over the entire frequency range of the WAVES spectrum; (2) a fast-drifting type II burst (in the frequency range 40–170 MHz, over the time interval of 11:07–11:17 UT) with a speed in the range 1000–1500 km s^{-1}; (3) another intense type II burst, but with a relatively slower speed (~400 km s^{-1}), between 500 and 250 MHz centered around 11:12 UT (seen as a broad pulse on the radio flux density profiles of 432, 410, and 327 MHz between 11:00 and 11:10 UT; see Fig. 5); (4) the onset of a moving type IV burst at 11:20 UT at frequencies below 400 MHz; (5) a narrow type III–like burst at ~11:15 UT in the WAVES portion of the spectrum; and (6) again in the WAVES spectrum, complex burst activities between 11:30 and 11:55 UT in the high-frequency part and a type III–like burst at 11:48 UT in the low-frequency region.

The type II and type IV bursts seen in the spectrum are also indicated by arrow symbols on the profiles of radio flux density measured with the NRH (Fig. 5). During the above metric burst activities, the Ondrejov radio measurements also showed intense emission over the extended high-frequency range, 800–4500 MHz. A strong impulsive emission observed at 3 GHz around 11:27 UT correlates with the second peak seen at the maximum of the X-ray intensity profile (refer to the *GOES* plot; Fig. 1).

The positional details of the above-mentioned metric radio bursts are derived from the NRH images. Both type II bursts, the slow- as well as the fast-drifting bursts seen in the dynamic radio spectrum of Tremsdorf, originate close to source A, which is shown in Figure 4 at a time just before the eruption. It may be noted that most of the transient activities are observed close to source A. Figure 7 shows the location of the type II bursts to be at the northwest side of source A. These images correspond to 164 and 236 MHz measurements at 11:09 and 11:14 UT and give the positions of the fast as well as the slow type II bursts. Source A and the type II burst appear to be a double source on the NRH image. These type II radio bursts also showed a marginal shift in position toward the northwest direction at P.A.s 280°–300°.

3. LASCO AND SCINTILLATION DATA: CME IN THE INTERPLANETARY MEDIUM

A large, fast "partial halo" CME moving toward the west side of the Sun was observed in white light by the LASCO/C2 and C3 coronagraphs on board the *SOHO* spacecraft. The C2 images cover a field of view of 2–6 $R_\odot$ and allow a better determination of the start time of the CME. The C3 coronagraph covers the corona up to ~30 $R_\odot$ (Brueckner et al. 1995). In the C2 field of view at ~3 $R_\odot$, the arrival of the CME was seen at 11:26 UT. Figure 8 shows a sequence of some images recorded by the C2 and C3 coronagraphs. The CME was fairly intense in white light, and it could be followed up to about 25 $R_\odot$; in this distance range, the CME propagated with a nearly constant speed of about 1000 km s^{-1}. A comparison of LASCO and Hα height-time data indicates that the detection of the CME in white light, around 11:26 UT at ~3 $R_\odot$, is at a much larger height than that of the Hα eruption recorded at the same time (refer to Fig. 3).

The propagation characteristics of the CME, at distances outside the LASCO field of view (>50 $R_\odot$), have been obtained from the remote sensing interplanetary scintillation technique (Manoharan et al. 2001). The scintillation measurements reported here have been obtained with the Ooty Radio Telescope, and the description of the method of observations and data reduction procedures has been given by Manoharan et al. (2000). It should be noted that the scintillation method detects the compression region (or sheath) between the shock moving ahead of the CME and the driver gas. Figure 9 shows the combined height-time plot made using the data from the Hα, white-light, and scintillation measurements. As indicated by the scintillation measurements, the CME decelerated at heights outside the LASCO field of view. Figure 10 illustrates the speed of eruption and that of the CME between the Sun and ~100 $R_\odot$ as derived from the Hα, white-light, and scintillation measurements. The Hα results show a rapid acceleration in the eruption speed. The CME speed of about 1000 km s^{-1} in the LASCO field of view decreases to a value of ~500 km s^{-1} at about 100 $R_\odot$ from the Sun. Further, the speed-distance dependence at distances $\geq$50 $R_\odot$ seems to follow a power-law relation, $V_{CME} \sim R^{-0.45}$.

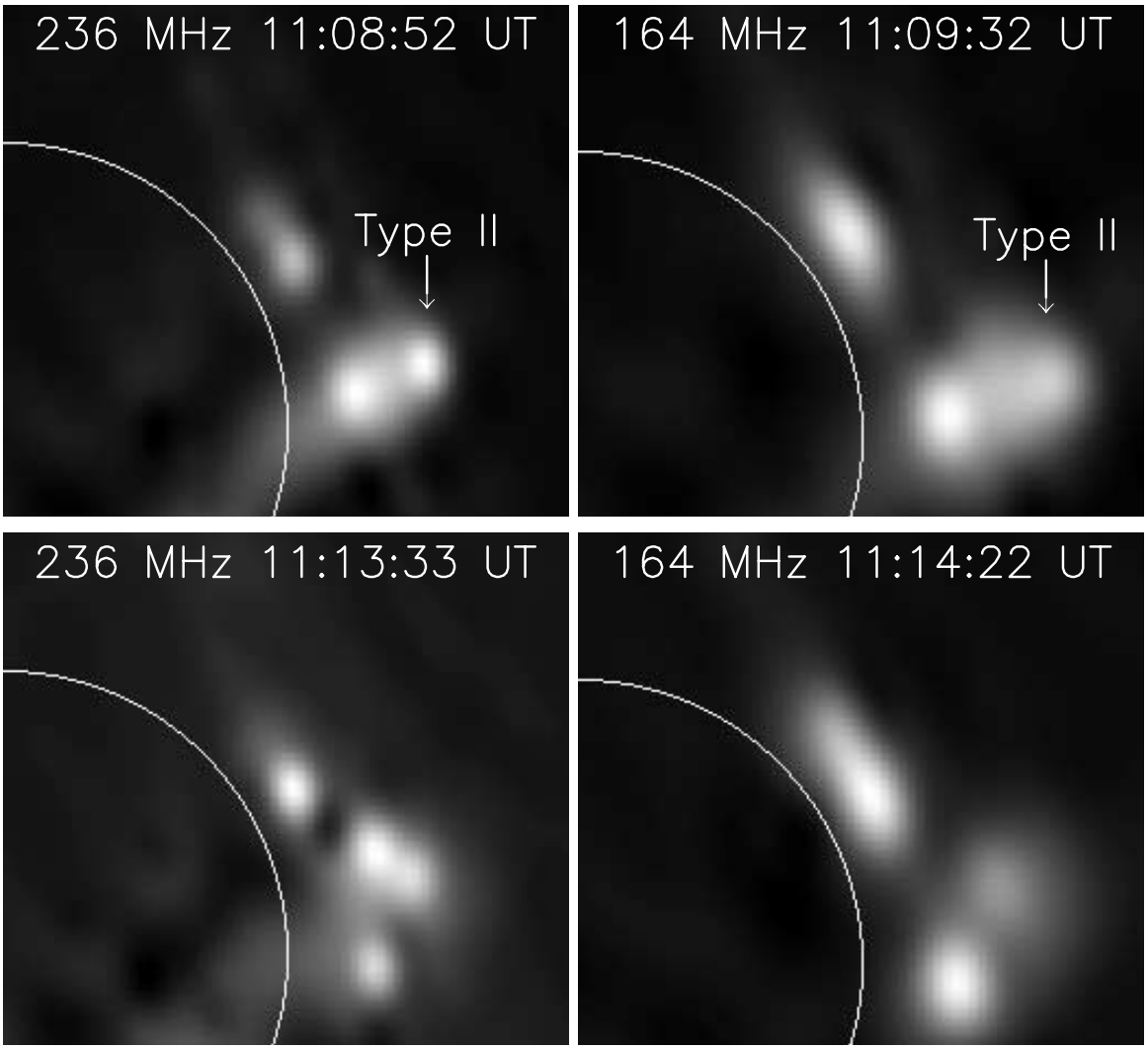

FIG. 7.—Northwest quarter of the radio images of the Sun showing the location of type II radio bursts at 164 and 236 MHz around 11:09 and 11:14 UT. [*See the electronic edition of the Journal for a color version of this figure.*]

4. DISCUSSION

The data set presented in this paper is perhaps unique in the sense that a detailed analysis provides a good understanding of the various stages of the eruption associated with the formation of a fast, large CME. From the typical size, density, and speed of the erupting cloud, we infer the energy associated with the eruption to be greater than $\sim 10^{30}$ ergs. This study emphasizes the importance of understanding the overall magnetic structure (or geometry) in the energy release process of a flare. The following images and measurements indicate the complexity of magnetic fields at NOAA AR 9393: (1) images from the EIT, (2) MDI magnetograms, (3) *Yohkoh*/SXT images taken before and after the flare, and (4) various radio burst activities during the eruption. In addition, the photospheric magnetic fields have been extrapolated on the basis of the force-free linear approximation method (e.g., Démoulin et al. 1997) to infer the coronal field conditions.

On 2001 April 2, the day of the event, however, the active region was close to the west limb, $\sim 65^\circ$ west. In general, when the active region is located at angular distances greater than 40° from the disk center, the extrapolation technique may not reveal the true connectivity of the field lines. Therefore, a magnetogram observed a few days prior to the CME was used in computing the overall three-dimensional coronal environment preceding the CME. Figure 11 shows the MDI magnetogram (*shown in contours*) superposed on an EIT image (*gray-scale plot*) of NOAA AR 9393 on March 29 at 11:12 UT (also see Fig. 4). The EIT image measured at 195 Å shows complex activity at the southwest portion of the active region, and some of the possible loops at the northeastern part are also seen in the image (see the portion of Fig. 11 bounded by coordinates $-100 \leq x \leq 10$ Mm and $0 \leq y \leq 100$ Mm). The computation of the force-free field extrapolation was performed using the FROMAGE software (G. Aulanier 2002, private communication),[5] and the results of the top projection view and the rotation of the active region to the location on the day of the event are shown in Figure 12. It is evident from the three-dimensional view of the magnetic field lines obtained from the extrapolation that a magnetic null point is located at the southwest part of the active region. The separatrix field lines, which

[5] Also see http://www.dasop.obspm.fr/fromage.

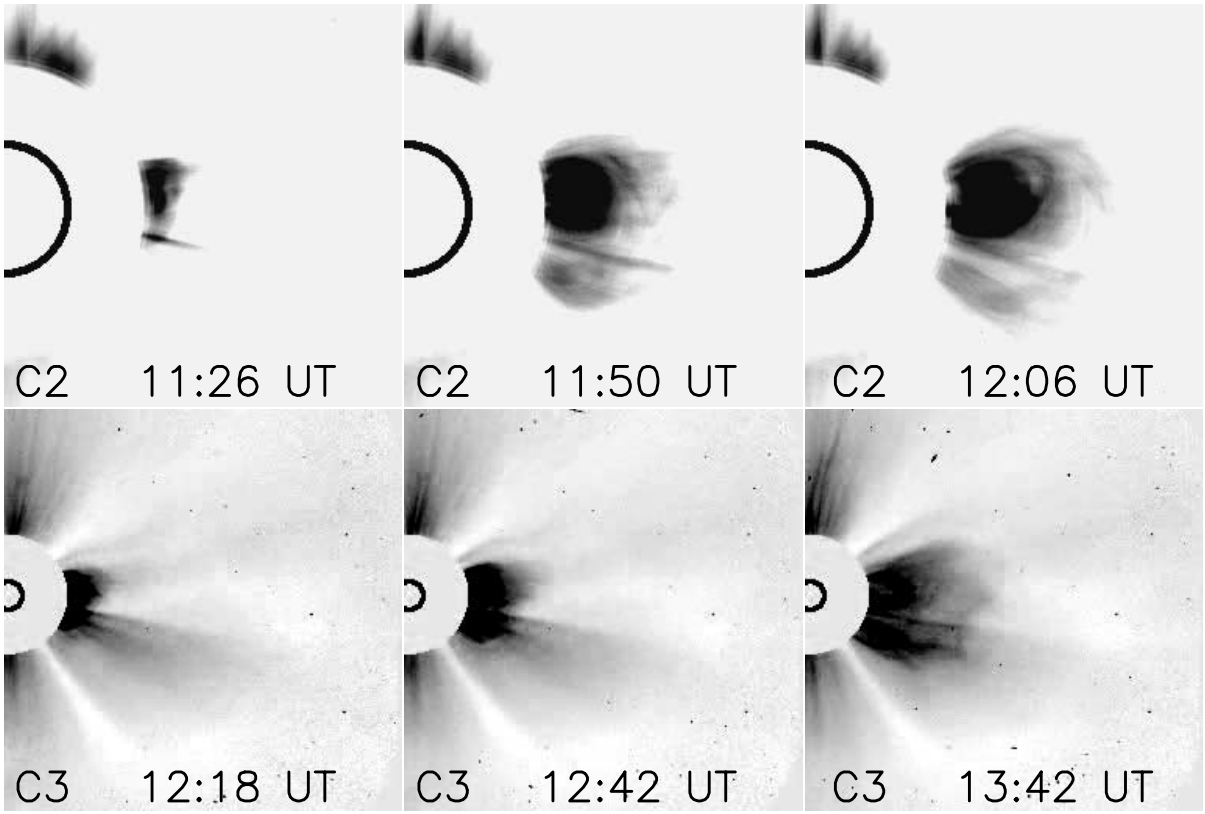

FIG. 8.—White-light images of the CME between 11:26 and 13:42 UT observed with the LASCO/C2 and C3 coronagraphs

originate or terminate at the null are shown as short loops, which are likely to be highly nonpotential (drawn in dark blue in the electronic version of the figure). These short loops stretch out to about a distance of ~25 Mm. The next level of field lines, however, extend away from the null to a greater distance, ~100 Mm, and they are shown by red. The large overlying magnetic field lines, which are also visible in the EIT and SXT data, are shown in green. (For color figures, refer to the electronic version of the paper.)

The above mentioned linear force-free extrapolation solution has been derived in the potential field approximation (e.g., Démoulin et al. 1997). Nevertheless, the deduced magnetic configuration is in excellent agreement with the extreme-ultraviolet and radio observations. For example, the system of loops seen in the EIT image (Figs. 4 and 11) has been nicely reproduced by the extrapolation as shown in Figures 11 and 12*a*. Further, the analysis of radio images (Figs. 4 and 7) with EIT data provides a guide to the understanding of the associated field configuration and to the release of energy above the separatrix at the magnetic null.

Taking into account the emission heights for the NRH images and their respective projections on the plane of the

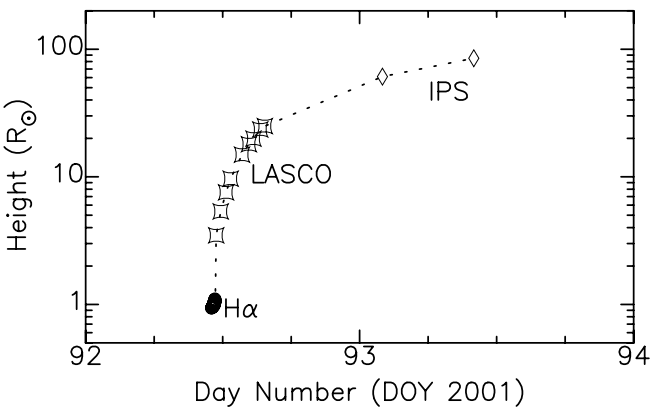

FIG. 9.—Height-time plot of the Hα eruption, the white-light data from LASCO, and the propagation of the CME measured by the interplanetary scintillation technique.

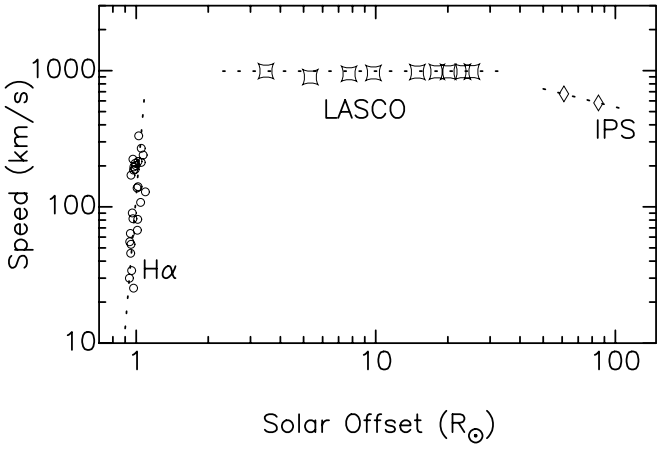

FIG. 10.—Speed-distance plot derived from the Hα, white-light, and scintillation measurements. A rapid acceleration in the Hα data, a nearly constant speed in the LASCO field of view, and the deceleration at distances of more than 40 $R_\odot$ are evident from the plot.

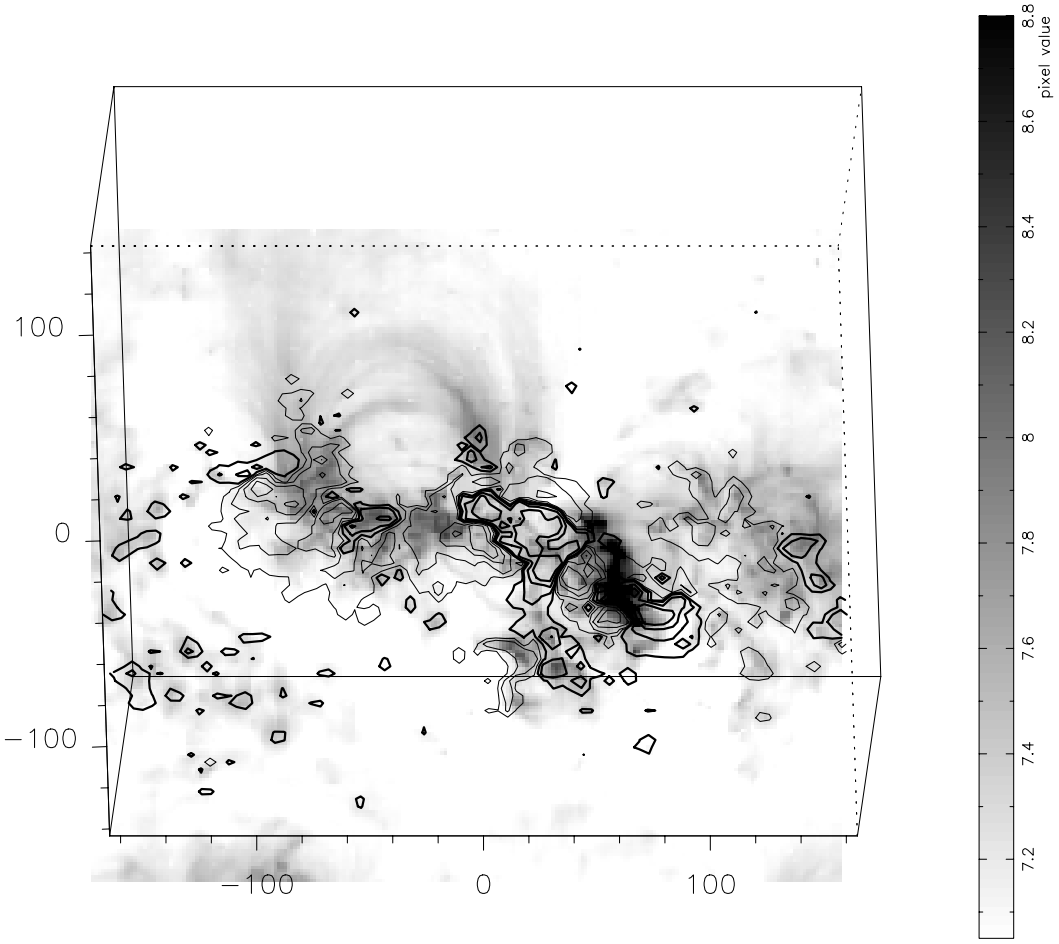

FIG. 11.—MDI magnetogram of NOAA AR 9393 superposed on the EIT image observed at 195 Å on 2001 March 29 at 11:12 UT. Each pixel on MDI is $\sim 2''$, i.e., $\sim$1450 km. The unit of x and y axes is in 10^6 m. The isocontours are 50, 100, 300, and 600 G, and positive contours are shown by thick lines and negative contours by thin lines. [*See the electronic edition of the Journal for a color version of this figure.*]

sky, the "frequency-height" profiles shown in Figure 4 provide an important clue on the geometry of the magnetic field involved in the eruption. It is inferred that the energy release has occurred at source A, radially below which the magnetic null is positioned. As shown in Figure 4, the systematic increase in separation between radio sources A and B as well as the height of source A indicate that these two sources correspond to the same system of loops running across the active region. At frequencies above 400 MHz, the emission has been observed just west of southwest edge of the active region and the absence of resolved source however at this location for most of the time indicates the complexity of the magnetic field configuration at low coronal heights. It is consistent with the low-lying loop structure of the separatrix or magnetic null revealed by the extrapolation. However, with decreasing frequency (or increasing height), the individual resolved sources have been observed and the systematic increase in height of source A (Fig. 4) (consistent with the typical "coronal height-plasma frequency" model; e.g., Bougeret, King, & Schwenn 1984) indicates that the loop originating at the southwest end of the active region is nearly due west and lies in the sky plane as viewed by an observer. On the other hand, the little or insignificant change observed in the position of source B with frequency suggests a twisted-loop leg that is nearly pointing to the observer. A similar configuration has also been revealed by the method of three-dimensional magnetic extrapolation as shown in Figure 12*b*.

Two stable sources observed before, during, and after the mass ejection at all frequency bands of the NRH (Figs. 4 and 7) thus coincide with the locations of (1) the low-level loop configuration of the separatrix or above the magnetic null (source A) and (2) twisted-loop shown across the active region (Fig. 12*b*; these field lines are shown by red in the electronic version of the figure) anchored at the northeast location (source B) (refer to Figs. 4, 7, and 12). The fast-moving ($\sim$1000 km s^{-1}) metric type II burst, the eruption of the cusplike loop seen in Hα at the southern edge of the active site, and the Moreton wave suggest a violent release of energy close to the chromospheric or the low coronal level. The formation of blobs of material may result from the reconnection process occurring between the rising of short loops below the separatrix and overlying loops, and it results in the formation and eventual ejection of the plasmoid. Further, the formation of blobs at increasing heights with time indicates that the reconnection point of the rising loops moves to larger heights with time. Moreover, the increase in the average speed of blobs formed one after another indicates that the energy involved in the eruption/reconnection increases with time and height. After the onset time of the CME, $\sim$11:02 UT, type III radio bursts observed close to the eastern edge of source A further confirm the

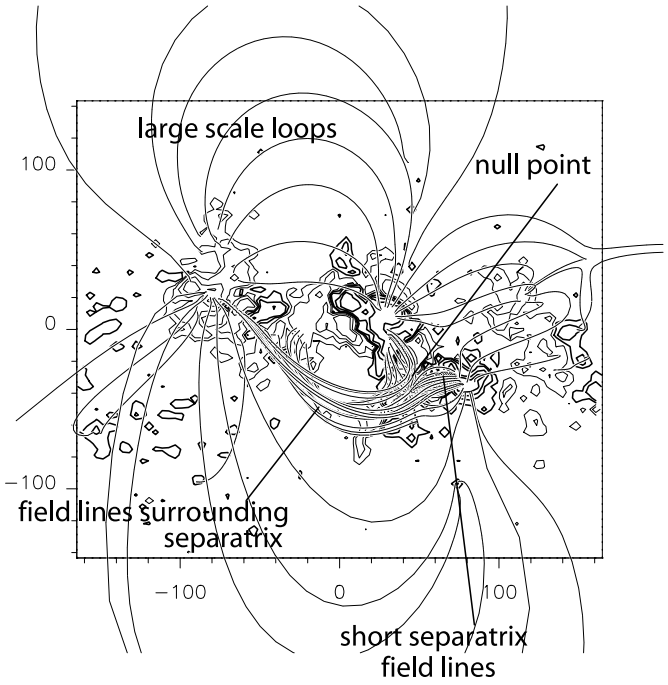

FIG. 12*a*

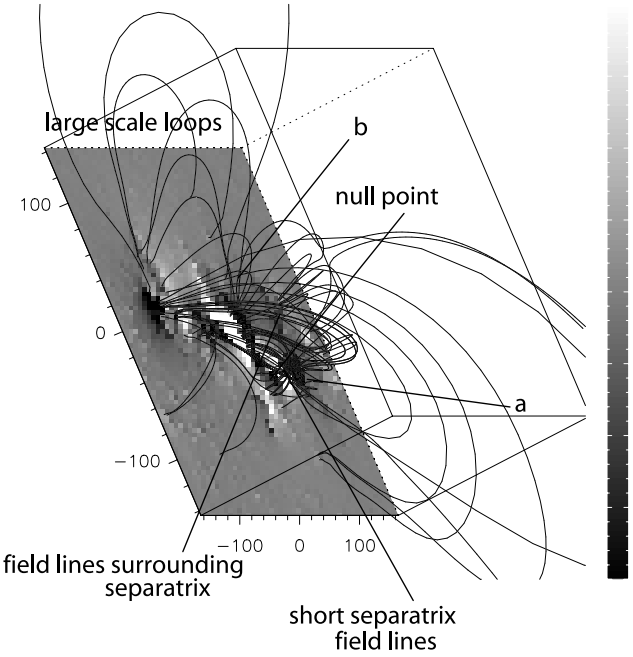

FIG. 12*b*

FIG. 12.—(*a*) Same as Fig. 11 including the force-free extrapolation of the magnetic field lines. The reduced large-scale loops are in good agreement with the EIT data (refer to Fig. 11). (*b*) Image (*a*) rotated to the location on 2001 April 2 at 11:00 UT indicates the possible magnetic configuration of the activity site associated with the CME eruption. A null point is located at the southwest edge of the active region. The approximate locations of radio sources A and B are also shown. [*See the electronic edition of the Journal for a color version of this figure.*]

opening of field lines for the acceleration of electrons at this location. This picture is consistent with the idea proposed by S. Antiochos and his coworkers (Antiochos et al. 1999; Aulanier et al. 2000). According to their model, when a magnetic null is placed high in the corona, the reconnection takes place across the separatrix and the accumulated energy in the lower atmosphere of the Sun blows out violently, i.e., a "breakout." The study of the Bastille Day eruption (e.g., Manoharan et al. 2001) with the help of magnetic extrapolation revealed the presence of a null point in the corona, and results provided evidence for the above model (Aulanier et al. 2000). The location and timing relationships of eruptive flares and their implications for the breakout model have also been considered by Sterling et al. (2001) and Sterling & Moore (2001).

The Moreton wave, observed during the Hα eruption, propagates tangentially to the south along the surface of the Sun with a speed $\leq$250 km s^{-1}, whereas the eruption as well as the material motion is toward the westward direction. In addition, as indicated by the radio (NRH and Tremsdorf) and Hα images, the Moreton wave and the type II radio bursts (to the west) seem to travel in different directions as well as with different speeds. The fast-drifting type II burst is likely to be due to a coronal shock wave that must have been produced at the time of magnetic energy release. The slow-drifting type II burst differs markedly from the above fast-moving one; it is possibly associated with the shock produced by the propagation of the CME. Similar results on short-lived, fast type II bursts associated with coronal blast waves (Gopalswamy et al. 1998; Klein et al. 1999) and bursts moving in the CME front (Maia et al. 2000) have been reported.

The occurrence height differs for the following features: (1) the onset of Moreton wave, (2) the slow-drifting type II burst observed at the high-frequency part of the spectrum, (3) the type III burst at 11:02 UT at frequencies below 160 MHz, and (4) the fast-drifting type II burst between 160 and 40 MHz. It suggests the height-time evolution of reconnection process at the time of mass ejection through the magnetic null above the active region. It is clearly evident from the NRH radio flux density profiles (Fig. 5) and from the radio spectrogram that the formation and onset of propagation of the slow-drifting type II burst mark the start of CME. The LASCO/C2 measurements projected back onto the Sun also are in agreement with the start time of the CME at 11 UT. The reconnection process and the subsequent opening of the field lines probably caused the narrow type III bursts seen in the WAVES dynamic spectrum around 11:15 UT in the height range of 2–3 $R_\odot$. The prolonged type IV radio burst observed after 11:20 UT must have resulted from the energetic electrons trapped in the outward-moving plasmoid.

The propagation speed of the CME in the interplanetary medium remains nearly constant at $\sim$1000 km s^{-1} at distances of less than 50 $R_\odot$ and declines as $V_{\rm CME} \sim R^{-0.45}$ at larger distances from the Sun. These speed measurements suggest that the energy associated with the CME is sufficient to prevent its deceleration in the solar wind up to about 50 $R_\odot$; however, at large heliocentric distance, when the CME loses a considerable amount of energy, it starts going through a rapid deceleration. At a certain stage, when the speed of the CME propagation nearly equals the speed of the solar wind flow, the CME may be carried by the solar wind. Although the propagation properties of the CME in the solar wind essentially depend on the conditions of the ambient solar wind, in the present case, the approximate change in the kinetic energy of the CME derived by the distance dependence relation is in good agreement with its

initial energy. The speed-distance results are also consistent with the earlier results obtained by Manoharan et al. (2001). They have shown that the power-law index of $V \sim R^{-\alpha}$ shows significant change with the initial speed or energy with which a CME gets launched into the interplanetary medium. That is, the power law is steeper for the high-speed CMEs than for the slow-speed cases (Manoharan et al. 2002).

The present study has provided a detailed account of the origin of the eruption and of the associated phenomena in the near-Sun region as well as propagation of the CME in the interplanetary medium. It may be noted that the same active region, NOAA AR 9393, during its passage on the solar disk has produced more than 25 flares stronger than M class in the soft X-ray classification scheme (refer to Fig. 1 for the soft X-ray classification). On the day of the present flare under discussion, the magnetic configuration of the separatrix around the magnetic null of the flare site released energy at two later intervals. The second peak near the maximum of the X-ray intensity profile (refer to Fig. 1) at 11:27 UT corresponds to an impulsive release of energy also seen in the microwave band and caused another wide CME with speed $\sim$725 km s^{-1}. The emphasis, however, is on the strongest flare, X20, of the current solar cycle and its associated CME, which hurled a large amount of high-energy particles into the interplanetary space from the same active region in the later part of the day. Thus, the study of such flare events associated with the similar magnetic structure is important not only for solar physics but also for the understanding of solar-terrestrial relations and space weather effects in the inner heliosphere.

The research at the University of Maryland is supported by NSF grant ATM 99-09809 and NASA grant NAG 5-8192. We thank J.-M. Malherbe (LESIA, Paris-Meudon Observatory) for kindly providing the Hα images and H. Aurass for the 40–800 MHz spectrum of the Astrophysical Institute Potsdam, Tremsdorf, Germany. We thank G. Aulanier (LESIA, Paris-Meudon Observatory) for making the magnetic field extrapolation computations. We acknowledge the team of ISTP *Wind*/WAVES and the *SOHO* consortiums of EIT, LASCO, MDI. The CME catalog is generated and maintained by the Center for Solar Physics and Space Weather, Catholic University of America, in cooperation with the Naval Research Laboratory and NASA. *SOHO* is an international collaboration between NASA and ESA. The magnetic field extrapolations used in this paper have been obtained from the code base FRench Online MAGnetic Extrapolations (FROMAGE). FROMAGE is a joint project between LESIA (Observatoire de Paris), CPhT (Ecole Polytechnique), and the Centre National d'Etudes Spatiales (CNES). The Nançay Radioheliograph is funded by the French Ministry of Education, CNRS, and Region Centre. We thank the referee for helpful comments.

REFERENCES

Antiochos, S. K., DeVore, C. R., & Klimchuk, J. A. 1999, ApJ, 510, 485
Aulanier, G., DeLuca, E. E., Antiochos, S. K., McMullen, R. A., & Golub, L. 2000, ApJ, 540, 1126
Bougeret, J.-L., King, J. H., & Schwenn, R. 1984, Sol. Phys., 90, 401
Brueckner, G. E., et al. 1995, Sol. Phys., 162, 357
Démoulin, P., Henoux, J. C., Mandrini, C. H., & Priest, E. R. 1997, Sol. Phys., 174, 73
Gopalswamy, N., et al. 1998, J. Geophys. Res., 103, 307
Hudson, H. 1999, in Solar Physics with Radio Observations, ed. T. Bastian, N. Gopalswamy, & K. Shibasaki (NRO Rep. 479; Nobeyama: Nobeyama Radio Obs.), 159
Kerdraon, A., & Delouis, J.-M. 1997, in Coronal Physics from Radio and Space Observations, ed. G. Trottet (Lecture Notes in Physics 483; Berlin: Springer), 192
Klein, K.-L., Khan, J. I., Vilmer, N., Delouis, J.-M., & Aurass, H. 1999, A&A, 346, L53
Kundu, M. R., Grechnev, V. V., Garaimov, V. I., & White, S. M. 2001, ApJ, 563, 389
Maia, D., Pick, M., Vourlidas, A., & Howard, R. 2000, ApJ, 528, L49
Manoharan, P. K., Gopalswamy, N., Yashiro, S., & Howard, R. A, 2002, Adv. Space. Res., submitted
Manoharan, P. K., Kojima, M., Gopalswamy, N., Kondo, T., & Smith, Z. 2000, ApJ, 530, 1061
Manoharan, P. K., Tokumaru, M., Pick, M., Subramanian, P., Ipavich, F. M., Schenk, K., Kaiser, M. L., Lepping, R. P., & Vourlidas, A. 2001, ApJ, 559, 1180
Moore, R. L., Sterling, A. C., Hudson, H. S., & Lemen, J. R. 2001, ApJ, 552, 833
Sterling, A. C., & Moore, R. L. 2001, J. Geophys. Res., 106, 25227
Sterling, A. C., Moore, R. L., Qiu, J., & Wang, H. 2001, ApJ, 561, 1116